Classification
Physics Abstracts
06.50 — 07.80 — 42.30

Practical limits of the deconvolution of images by kriging(*)

Dominique Jeulin and Didier Renard

Ecole des Mines de Paris, Centre de Géostatique, 35 rue Saint-Honoré, 77305 Fontainebleau, France

(Received March 05, 1992; accepted July 09, 1992)

Résumé. — En analyse d'image, les données accessibles ne sont généralement pas de support ponctuel, mais convoluées par une fonction de pondération $p(x)$, déterminée par le processus physique du mode de prélèvement. La déconvolution des images est traitée généralement par transformation de Fourier. Il est bien connu que cette approche est inopérante dans le cas de données bruitées après convolution, de données non disponibles à maille régulière et lorsque des données manquantes doivent être interpolées. C'est pourquoi il est préférable de suivre une autre démarche basée sur une procédure d'estimation des données ponctuelles par krigeage déconvoluant. Les limites pratiques de cette méthode peuvent s'exprimer en termes de variance d'estimation (ou encore de rapport signal sur bruit) accessible pour chaque situation expérimentale après modélisation. Elles sont illustrées par des cas pratiques de fonction de pondérations $p(x)$ et de variogrammes, à partir de calculs et de simulations.

Abstract. — In image analysis, the available data do not usually have a point support, but are convoluted by a weighting function $p(x)$, which is determined by the physical process of the sampling mode. Deconvolution of images is generally treated by Fourier transform. This approach is known to be inoperable when considering convoluted data with noise or when a regular grid of data is not available and therefore missing data have to be interpolated. It is for this reason that it is better to use another system based on the process of estimating point data by deconvoluting kriging. The practical limitations of this method can be expressed in terms of variance of estimation (or of signal to noise ratio), accessible for each experimental situation after modeling. They are presented by practical cases of the weighting function $p(x)$ and variograms $\gamma(h)$, from calculations and simulations.

1. Introduction.

In many circumstances, such as in image analysis (electron images, X-ray images in the microprobe,...), the available data are not with a point support, but are convoluted by a weighting function. This last function depends on the underlying physical process and can be established from theoretical considerations, or can be measured with appropriate experiments. When the support of the weighting function is larger than the imaged features, this results in blurred images, sometimes degraded by additional noise, that require some restoration before any further processing.

(*) Another version of this paper was published in Cahiers de Géostatique, Fasc. 1, Compte-rendu des Journées de Géostatique, Paris School of Mines, 1991.

After recalling the available deconvolution methods, we develop a deconvolution procedure based on kriging, with the aim of exploring its implementation together with its efficiency and its limits in the presence of noise. This work is illustrated by computer calculations and simulations.

2. Recapitulation of deconvolution methods.

In this part, we introduce the various approaches that enable images to be deconvoluted. All these approaches are very common in the image analysis literature (see [1] for instance). However there is little discussion of their efficiency and their limitations, as will be presented in the next part of this paper using simulated images.

2.1 NOTATION. — We consider a pure signal (or an image in $\mathbb{R}^n$) $Y(x)$ which is modified through a convolution by a weighting function $p(x)$. In this paper $p(x)$ is normalized, so that its integral over spatial coordinates is equal to 1, and $\check{p}(x) = p(-x)$. Experimentally, if N designates a noise term uncorrelated to the signal Y, we observe the data:

$$Z = Y * \check{p} \quad \text{(noise-free)} \tag{1}$$

or

$$Z = Y * \check{p} + N \quad \text{(additional noise)} \tag{2}$$

Such a situation is common in the following experimental fields: electron microscopy [2], electron microprobe analysis [3], optical confocal microscopy [4-6].

Knowing the weighting function p, the problem is to estimate the underlying image $Y(x)$ at each pixel x from the data $Z(x_\alpha)$ known at pixels x_α, and the properties of the noise. This can be done by two different approaches, namely the implementation of a Fourier transform or an estimation of the underlying signal by kriging. The two approaches are briefly recalled below.

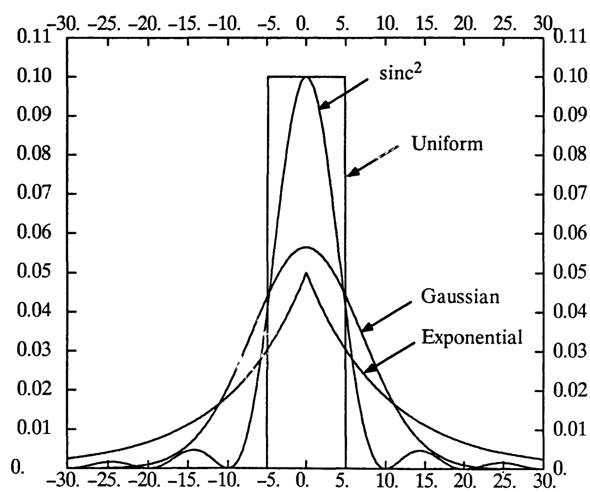

Fig. 1. — Different convolution weighting functions with the same diameter 10.

We limit our discussion to 1-D convolution functions for the sake of simplicity as explained in the practical study presented in [4-6]. In practice the following weighting (or "convolution") functions (see Fig. 1) are common to various physical situations:

- uniform convolution function (for instance blur caused by a lack of focus) with diameter d :

$$p(x) = \frac{1}{d} \text{ for } |x| < \frac{d}{2}, \text{ 0 otherwise}$$

- exponential convolution function:

$$p(x) = \frac{1}{2d}\exp\left(-\frac{|x|}{d}\right)$$

- Gaussian convolution function (for instance in electron microscopy):

$$p(x) = \frac{1}{d\sqrt{\pi}}\exp\left(-\frac{|x|^2}{d^2}\right)$$

- convolution function derived from the sinc function:

$$p(x) = \frac{1}{d}\left(\frac{\sin\dfrac{\pi|x|}{d}}{\dfrac{\pi|x|}{d}}\right)^2$$

Similarly n-dimensional convolution functions can be defined (in the isotropic case we replace $|x|$ by the radius r).

2.2 Deconvolution by the Fourier transform. — In the case of the pure convolution, it is easy to achieve an exact deconvolution by means of the Fourier transform, from the application of the so-called convolution theorem: if $F(Y)$ and $F(p)$ represent the Fourier transform respectively of the signal $Y(x)$ and of the convolution function $p(x)$, we have the following result in the case corresponding to equation (1):

$$F(Z) = F(Y) \cdot F(p) \tag{3}$$

From (3) it is easy to compute the unknown Y according to the following steps:

- calculation of the two Fourier transforms $F(Z)$ and $F(p)$ from the data Z and from the known convolution function p
- calculation of $F(Y)$ from equation (3)
- calculation of Y by an inverse Fourier transform

This well-known procedure is used in [7], among other examples, to improve confocal microscope images.

However, it suffers serious drawbacks:

- Its implementation is limited to data on a regular grid of points (this is not a real difficulty in image analysis), but is impracticable in the case of irregular sampling grids.
- The transform $F(p)$ may be equal to zero for certain frequencies.
- A major limitation of the use of the Fourier transform results from the fact that the deconvolution is an unstable operator, that will tend to increase the slightest errors on the knowledge of the data Z [1, 8]. In particular, in the presence of noise, the estimated Y is completely different from the underlying signal, which cannot be recovered by this method. This can be regarded as a consequence of the fact that an image resulting from a convolution is expected to be reasonably smooth, which is not consistent with the presence of noise, even at a low level.

2.3 DECONVOLUTION BY KRIGING. — A powerful method for filtering or interpolating missing data, called kriging, has been developed in the frame of geostatistics [9, 10]. This procedure was developed in the fifities to estimate unknown or noisy data, accounting for information on the spatial structure of the underlying phenomena. The early applications of geostatistics were devoted to the estimation of local concentrations in orebody deposits from a set of data obtained on probes at different locations. The term kriging was coined in honour of Dr. D. Krige, who initiated this method of estimation for gold deposits. As will be seen below, it involves the estimation of the unknown data by a local linear regression. Recently, applications to image analysis have been proposed: the case of multivariate images obtained from an electron microscope or from a microprobe are presented in [2, 3]. Non linear filters have also been developed to estimate local histograms [13, 14], using disjunctive kriging [15]. Here we consider the common case of a single datum per pixel x, such as the recorded light intensity $Z(x)$, deriving from an underlying (pure) signal $Y(x)$. The variables $Y(x)$ and $Z(x)$ are assumed to have the same mean and to be realizations of an intrinsic 3D random function: the increments $Z(x+h) - Z(x)$ are a second order stationary random function. If the symbol E is used for the mathematical expectation, we define the variogram of the random function Z as follows:

$$\gamma_Z(h) = \frac{1}{2}\mathrm{E}\left[(Z(x+h) - Z(x))^2\right] \tag{4}$$

The variogram is estimated from the data, replacing the expectation in equation (4) by the mean squared differences over the pairs x, $x+h$. Examples are given in figure 6. To restore the underlying variable Y from the observed variable Z, we use as an estimator $Y^*(x)$, a linear combination of the data in a neighbourhood of x (pixels x_α) :

$$Y^*(x) = \sum_\alpha \lambda^\alpha Z(x_\alpha) \tag{5}$$

The weights in equation (5) are the unique solution of the linear system (6) below (commonly referred to as the kriging system) obtained from an unbiased and a minimal variance estimator:

$$\begin{aligned} &\sum_\alpha \lambda^\alpha \gamma_Z(x_\alpha - x_\beta) + \mu = \gamma_{YZ}(x - x_\beta) \\ &\sum_\alpha \lambda^\alpha = 1 \end{aligned} \tag{6}$$

where γ_{YZ} is a cross-variogram:

$$\gamma_{YZ}(h) = \frac{1}{2}\mathrm{E}[(Y(x+h) - Y(x))(Z(x+h) - Z(x))] \tag{7}$$

The variance of the estimate is given by $\mu + \sum_\alpha \lambda^\alpha \gamma_{YZ}(x_\alpha - x)$.

As seen from equation (6) the optimal filter, which is a generalization of the Wiener filter, depends on the structure of the data via the variograms. When using the variogram of an image, the weights λ^α of equation (5) do not depend on the location of the neighbourhood. This is well-suited to stationary data. Local variograms can be used in subimages, at the expense of a lack of robustness. For nonstationary data, it is better to introduce nonstationary models such as intrinsic random functions of order k, for which the weights satisfy additional conditions to equations (6)

[16]. Such models are of constant use in applications to cartography. They can be introduced for deconvolution as well. In the context of images, we encounter the following situations:

i) interpolation of a pure signal.

ii) filtering a noisy signal Z (with appropriate assumptions on the noise [3]): $\gamma_{YZ} = \gamma_Y$ estimated from γ_Z.

iii) deconvolution: we have

$$\gamma_Z = \gamma_Y * P - I(P), \quad \gamma_{YZ} = \gamma_Y * p - I(p), \quad I(P) = \int \gamma(u)P(u)\mathrm{d}u \text{ and } P = p * \check{p}$$

This deconvolution algorithm is an alternative to the Fourier transform method mentioned previously, and has already been proposed in [11, 12]. In the presence of noise, γ_Z presents a discontinuity as $\gamma_Z = \gamma_Y * P - I(P) + C_o$ for $h \neq 0$ where C_o is the variance of the noise.

iv) any combination of the previous situations.

In each case we use theoretical models of variograms for γ_Y, from which γ_Z is calculated and compared to the experimental γ_Y. This is illustrated in the next part. When the variance of Y is finite, the quality of the estimator is measured from the calculation of the signal to noise ratio $\mathrm{SNR} = \sigma_Y^2/\sigma_K^2$, to be compared with the raw $\mathrm{SNR}_0 = \sigma_Y^2/\sigma_\epsilon^2$, where $\epsilon = Y - Z$ and:

$$\sigma_\epsilon^2 = \mathrm{Var}(Y - Z) = 2I(p) - \int\int p(x)p(y)\gamma(x-y)\mathrm{d}x\mathrm{d}y$$

In practical situations the calculated SNR depends on the choice of the variogram model (through the expression of the variance of estimation σ_K^2).

Some comments on deconvolution by kriging may be useful here:

- the kriging procedure is itself a convolution, which may seem to be a paradox ! However, this is expected since we are looking for an inverse of a linear operator that is invariant under translation. Furthermore, since we will get positive and negative weights for a pure deconvolution (Fig. 4 and Tab. II), it is more correct to compare it to a differentiation. Therefore, it is expected to favour instabilities in the presence of noise.
- It can be shown [8] that, without the last condition of equation (6), unlike the Fourier transform procedure, kriging is stable against perturbations of the data Z by noise ϵ. This operation belongs to the class of regularization operators for the ill-posed problem of deconvolution [8].
- The connection between the two approaches can be understood in the case of a pure deconvolution.

For a stationary random function Y with covariance $C_Y(h)$ and known expectation, the cokriging system (6) can be written as follows [9, 10], if we consider a weighting measure λ instead of the discrete set of weights λ_α of equation (5):

$$Y^*(y) = \lambda * Z(y)$$

The measure λ should satisfy the system (8):

$$\lambda * C_Z(x) = C_{YZ}(x - y) \tag{8}$$

for every point x in $\mathbb{R}^n$. As we are considering a stationary random function Y, the measure λ is the same for each point y, so that we can restrict the system (8) to $y = 0$. Then:

$$\lambda * C_Z(x) = C_{YZ}(x) \tag{8bis}$$

In (8bis), the covariances C_Z and C_{YZ} are deduced from the covariance C_Y by:

$$C_Z = C_Y * P, \quad C_{YZ} = C_Y * \check{p}$$

By taking the Fourier transform of equation (8), we get:

$$F(\lambda) \cdot F(C_Z) = F(C_{YZ})$$
$$F(\lambda) \cdot F(C_Y) \cdot F(p) \cdot F(\check{p}) = F(C_Y) \cdot F(\check{p}) => F(\lambda) = \frac{1}{F(p)}$$

and from $Y^* = \lambda * Z$:

$$F(Y^*) = \frac{F(Z)}{F(p)}$$

which from equation (3) shows that in this case the estimator Y recovers the exact function Y. Therefore for a pure deconvolution of a stationary random function, the two approaches (deconvolution by Fourier transform and by kriging) are equivalent. As a consequence the measure λ does not depend on the covariance C_Y, which is different in the presence of noise. We will see later that this is nearly satisfied in practical examples for discrete neighbourhoods.

Usually, as for instance for the weighting functions used in this paper, the Fourier transform $F(\lambda)$ deduced from $F(p)$ has no inverse, so that the cokriging system (6) is unstable in the absence of noise. For a pure white noise C_0 (called a nugget effect) on the covariance of the data Z, we have:

$$C_Z = C_Y * P + C_0 \cdot \delta$$
$$F(C_Z) = F(C_Y) \cdot F(p) \cdot F(\check{p}) + C_0$$

so that by Fourier transform, we can deduce from (8):

$$F(\lambda) = \frac{F(C_Y) \cdot F(\check{p})}{F(C_Y) \cdot F(p) \cdot F(\check{p}) + C_0} \tag{9}$$

The function $F(\lambda)$ defined by equation (9) usually posseses an inverse Fourier transform, from which the measure λ can be recovered. Therefore, a numerically stable solution of the cokriging system is obtained by introduction of a slight nugget effect for the pure deconvolution problem.

Other authors purpose deconvolution algorithms based on iterative constrained procedures with a regularization [17, 18]. An interesting application to confocal microscopy images is given in [19]. In order to make an objective comparison of the methods, the same data sets would have to be processed, such as the simulations used in this paper, so as to estimate the improvement of the SNR ratio.

2.4 PRACTICAL IMPLEMENTATION OF DECONVOLUTION BY KRIGING. — In practical applications, deconvolution by kriging requires us to solve the cokriging system after a so-called structural analysis from which the underlying variogram γ_Y can be identified. The direct calculation of γ_Y from γ_Z and p is again a deconvolution, which is unstable according to the experimental fluctuations of the variogram. A much better approach lies in the use of variogram models depending on parameters. The procedure may be split into the following steps:

i) Calculation of the experimental variogram γ_Z from the data Z. This variogram should show a nugget effect in the presence of noise, followed by a very regular behavior for small separations h, due to the convolution function p.

ii) Choice of a model for the underlying variogram γ_Y, with a possible decomposition into various scales. We use theoretical models from *a priori* knowledge of the structure and from the behaviour of the experimental variogram γ_Z.
iii) Calculation (mostly by numerical means) of a theoretical γ_Z and from p. We must point out that if p is unknown, the model γ_Y is undetermined, so that no correct deconvolution can be expected.
iv) Comparison between the experimental and the model variogram γ_Z. If necessary, correction of the model (continuation of steps ii)-iii)-iv)).
v) Choice of the optimal neighbourhood based on the calculation of the SNR. Numerical calculation of the solution of the cokriging system (6). Restoration of the image from the system of weights and calculation of the quality of the deconvolution from the SNR coefficients.

This procedure, which is implemented in a software package developed by Renard [20], is illustrated and evaluated on simulations in parts 3 and 4.

3. Implementation of deconvolution by kriging.

In this part, we present the effect of the convolution on the variograms and on the expected SNR improvement for some examples.

3.1 STRUCTURAL ANALYSIS. — Deconvolution by kriging and noise filtering require a prior study of the continuity and the regularity of the target variable, known as its "structure".

The structure of the measured data variable Z may be a second order stationary random function, more regular than Y (as it is smoothed by p).

The principle is to calculate the experimental variograms (possibly in several directions). Then, using a graphics fitting program, we try to fit both the theoretical model of the underlying variable and the convolution weighting function to each directional experimental variogram. In practice, this problem cannot be solved. Usually the convolution weighting function is known (as it is linked to the experimental tool) and the only problem is to fit the structure of the underlying variable.

We illustrate the effect of the convolution on a spherical variogram:

$$\gamma(h) = C\left(\frac{3h}{2a} - \frac{h^3}{2a^3}\right) \text{ if } h \leq a, \; C \text{ otherwise}$$

where "a" stands for the range (or zone of influence) and C is the sill (corresponding to the flat part of the variogram) which should coincide with the global dispersion variance of the image.

Figure 2 shows a 1-D spherical variogram (range = 15, sill = 1) and its behaviour when convoluted by a uniform weighting function with diameter equal to 1, 2, 5, 10 and 15 respectively. We note the smooth behaviour of the variogram at the origin, which corresponds to a continuous variable obtained by convolution; the range of the convoluted variogram corresponds to the range of the initial spherical variogram incremented by the radius of the convolution weighting function, as expected.

In figure 3, we have represented the theoretical 2-D spherical variogram (the same as in the previous example) altered by a 1-D convolution weighting function (along X only) with the same diameters as previously. The variograms are represented along X and along Y. The effect of the convolution vanishes when we move from the X to the Y direction although it does not disappear completely.

The final problem that may arise comes from the method used to calculate the function $\gamma^* P$. Because of the large number of possible variograms and convolution functions, a formal integration is usually abandoned. Instead we dicretize the convolution weighting function and multiply this weight by the value of the variogram for the corresponding distance.

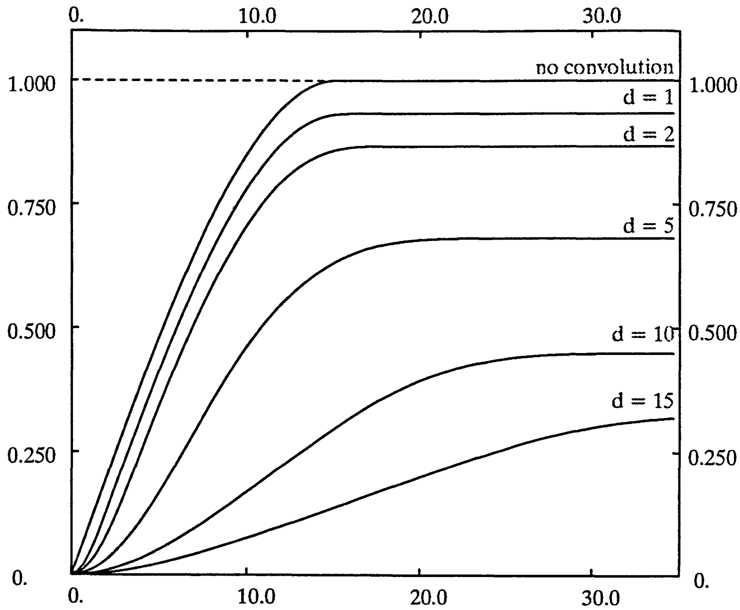

Fig. 2. — 1-D Spherical variogram (Range 15; Sill 1). 1-D Uniform convolution function (Diameter *d*).

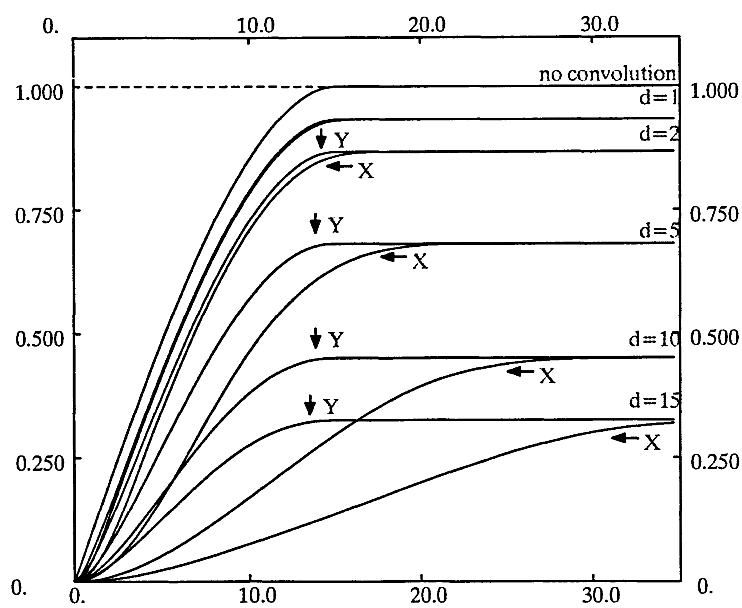

Fig. 3. — 2-D Spherical variogram (Range 15; Sill 1). 1-D Uniform convolution function along X (Diameter *d*).

This discretization must be carried out with a large number of fine steps. Moreover, the convoluted variogram must remain an "authorized" variogram, which implies a careful choice of the discretization procedure to maintain the non-negative definiteness property of the resulting structure.

3.2 DECONVOLUTION KRIGING AND NOISE FILTERING. — When the structure is determined, the kriging process can be initiated. Then a second problem arises, which is linked to the choice of the neighbouring information. As we work on regular 2-D isometric grid data sets, we have selected to work on neighbourhoods centred on the target grid node, characterized by their extension counted in grid nodes along each direction $(N_x,\ N_y)$ or rather their radius $(R_x,\ R_y)$ where $N_x = 2\ R_x + 1$. In order to simplify the algorithm, we will simply not process the target grid nodes located too close to the edge (less than the neighbourhood radius) so that the neighbourhood of each target node effectively processed is complete. Therefore, when the radius is chosen, the kriging weights remain the same for all the target nodes processed and the kriging operation is reduced to a simple scalar product between the pre-calculated weights and the values of the grid nodes neighbouring the target node.

From the choice of a model for $\gamma_Z(h)$, we can calculate the variances σ_Y^2, σ_K^2 and σ_ϵ^2. They are used to estimate signal to noise ratio.

3.2.1 *Study of the signal to noise ratio.* — The signal-to-noise improvement corresponds to the following ratio:

$$I(R) = \frac{\mathrm{SNR}}{\mathrm{SNR}_0} = \frac{\sigma_\epsilon^2}{\sigma_K^2}$$

The optimal neighbourhood radius R is the one for which the signal-to-noise improvement flattens. In other words, we look for a horizontal asymptote in the graph of $I(R)$. This is illustrated by the following example: working in one dimension space, and considering two basic underlying variograms (the spherical and the cubic variograms) with the same range (15) and the same sill (1). The cubic variogram is given by:

$$\gamma(h) = C\left(\frac{7h^2}{a^2} - \frac{35h^3}{4a^3} + \frac{7h^5}{2a^5} - \frac{3h^7}{4a^7}\right) \quad \text{if } h \leq a, \ C \text{ otherwise}$$

We have established graphs of $I(R)$ for various amounts of nugget effect (0.01, 0.05, 0.1), for different convolution weighting functions (uniform, exponential and Gaussian) and for several diameters of these functions (1, 2, 3, 5 and 10). In addition to the graphs, we also provide numerical results for the SNR_0 and SNR scores, as well as the asymptotic $I(R)$ (see the Appendix).

Several points emerge from these calculations:

- when $R = 35$, almost all the curves $I(R)$ have reached their asymptote. The only exception comes from the uniform convolution function with a large diameter ($d = 10$) where $R = 50$ would be more appropriate: this is due to the fact that the uniform convolution function works as an equally weighted moving average of the image whereas all the other convolution functions give a larger weight to the central point than to the peripheral ones.
- the more regular the underlying variogram (for the same amount of nugget effect), the larger the SNR_0, the SNR and the improvement $I(R)$.
- in the presence of noise, the SNR and SNR_0 are higher for the uniform convolution function than for the other convolution functions: this is due to the lower degradation of the signal since the uniform convolution function is more "local" for a given value of d (see Fig. 1).

As an example, we compare the results obtained with an underlying spherical variogram (case 1) and an underlying cubic variogram (case 2), for the same nugget effect ($C = 0.1$), for different convolution functions with the same diameter ($d = 3$) (see Tab. I).

Table I.

exponential	case 1)	SNR0 = 3.86	SNR = 6.42	I(R) = 1.66
	case 2)	SNR0 = 5.01	SNR = 14.74	I(R) = 2.94
gaussian	case 1)	SNR0 = 4.13	SNR = 6.76	I(R) = 1.64
	case 2)	SNR0 = 6.03	SNR = 18.33	I(R) = 3.04
uniform	case 1)	SNR0 = 4.95	SNR = 8.32	I(R) = 1.68
	case 2)	SNR0 = 8.29	SNR = 25.62	I(R) = 3.09

3.2.2 *Study of the kriging weights.* — All the previous calculations have been performed with some nugget effect (from 0.01 to 0.1). In practice, the structure of the convoluted variable is usually very smooth (specially when using the uniform weighting function) and therefore the weights of the "pure" deconvolution kriging system and sometimes even the signal to noise ratios are unstable. The traditional solution is to add some artificial nugget effect (which does not reflect the nature of the underlying variable) in order to solve the pure deconvolution problem.

However (at least in theory), when no nugget effect is added, the weights do not depend on the underlying variogram, but only on the characteristics of the convolution weighting function.

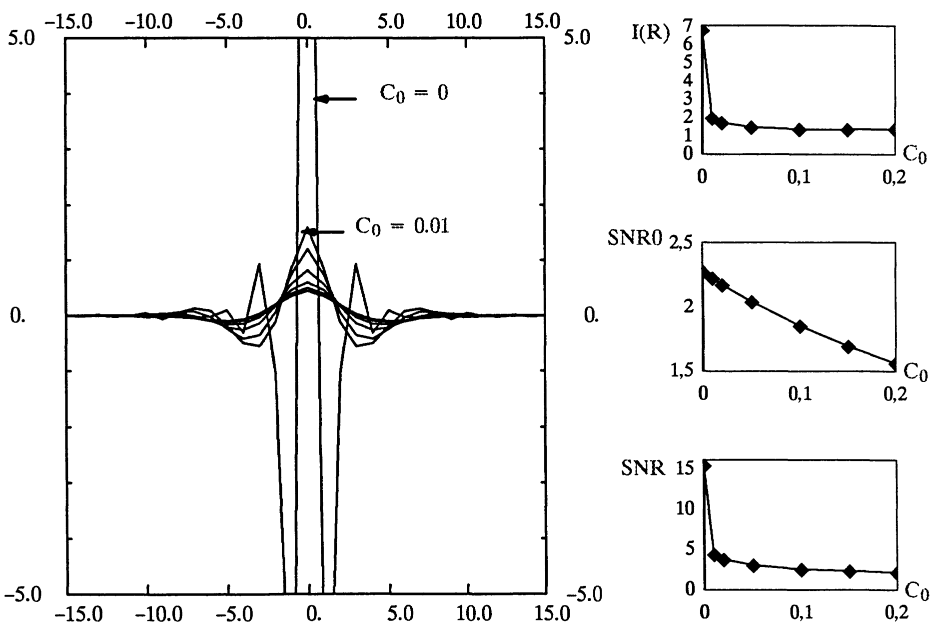

Fig. 4. — Influence of the nugget effect C_0 on the deconvolution kriging weights.

Figure 4 shows the effect of the nugget effect on the kriging weights. It is obtained for a fixed neighbourhood ($R = 15$) with an underlying spherical variogram (Range 10; Sill 1), for an exponential convolution weighting function (Diameter 3). The different values of the nugget effect are 0., 0.01, 0.02, 0.05, 0.1, 0.15 and 0.2. For an increasing nugget effect, the weights tend to be more uniform, since the smoothing of the data required by the noise becomes more effective.

Table II is obtained for an underlying spherical variogram (Range = 5; Sill = 1) and for an exponential convolution weighting function (Diameter = 3). This corresponds to SNR0 = 2.271. It shows the effect of the neighbourhood radius R on the pure deconvolution kriging weights and on the signal to noise ratio improvement: R varies from 1 to 20. Because of the symmetry, only half of the weights are listed, the first value corresponding to the central weight.

As illustrated from the $I(R)$ variations, the optimal radius is reached at $R = 6$. We also notice that the kriging weights obtained for $R = 6$ will not vary significantly up to $R = 20$.

Table II.

R	1	2	3	4	5	6	7	8	9	10
I(R)	6.662	6.707	6.762	6.776	6.776	6.776	6.775	6.776	6.777	6.778
λ	20.105	21.562	20.926	20.890	20.881	20.883	20.887	20.891	20.883	20.885
	-9.553	-10.620	-9.758	-9.578	-9.569	-9.573	-9.575	-9.579	-9.573	-9.571
		0.339	-0.566	-1.010	-1.046	-1.044	-1.042	-1.040	-1.044	-1.048
			0.361	0.820	0.913	0.923	0.920	0.922	0.923	0.926
				-0.177	-0.277	-0.309	-0.311	-0.314	-0.314	-0.314
					0.039	0.074	0.088	0.090	0.088	0.087
						-0.013	-0.031	-0.031	-0.019	-0.020
							0.007	0.006	-0.019	-0.027
								0.001	0.025	0.052
									-0.009	-0.041
										0.013

R	11	12	13	14	15	16	17	18	19	20
I(R)	6.775	6.776	6.777	6.777	6.777	6.777	6.776	6.777	6.776	6.776
λ	20.883	20.878	20.882	20.875	20.875	20.879	20.881	20.887	20.890	20.877
	-9.566	-9.568	-9.570	-9.562	-9.561	-9.568	-9.575	-9.577	-9.579	-9.572
	-1.054	-1.049	-1.047	-1.050	-1.055	-1.045	-1.039	-1.040	-1.039	-1.042
	0.931	0.927	0.928	0.924	0.931	0.923	0.921	0.922	0.920	0.921
	-0.316	-0.315	-0.318	-0.311	-0.319	-0.316	-0.314	-0.313	-0.311	-0.313
	0.085	0.087	0.090	0.083	0.091	0.091	0.087	0.085	0.086	0.086
	-0.015	-0.019	-0.022	-0.016	-0.021	-0.022	-0.017	-0.015	-0.020	-0.018
	-0.032	-0.028	-0.024	-0.030	-0.028	-0.026	-0.030	-0.031	-0.026	-0.029
	0.064	0.061	0.059	0.063	0.062	0.060	0.061	0.062	0.059	0.062
	-0.067	-0.067	-0.067	-0.069	-0.068	-0.067	-0.067	-0.067	-0.065	-0.068
	0.041	0.046	0.043	0.044	0.043	0.043	0.043	0.041	0.041	0.043
	-0.011	-0.017	-0.008	-0.006	-0.004	-0.005	-0.005	-0.004	-0.003	-0.004
		0.003	-0.007	-0.017	-0.018	-0.018	-0.018	-0.018	-0.019	-0.019
			0.004	0.014	0.017	0.017	0.016	0.016	0.017	0.017
				-0.004	-0.007	-0.005	-0.003	-0.004	-0.004	-0.004
					0.001	-0.001	-0.004	-0.004	-0.004	-0.004
						0.001	0.004	0.004	0.004	0.004
							-0.001	-0.002	-0.001	0.000
								0.000	-0.001	-0.002
									0.000	0.001
										0.000

4. Application.

In this part, we illustrate the theoretical results discussed previously by considering simulated data sets for which all the structural and the convolution function characteristics are known. The exercise is used to establish the validity of the inference method of the underlying variogram and to evaluate the performance and the limitations of the kriging procedure for deconvoluting and filtering noise.

4.1 THE SIMULATED DATA SET. — For this data set, all the underlying structure and the convolution function characteristics are known. Although no theoretical limitation holds, we have chosen to perform this study on 2-D images (256 x 256 pixels) both for efficiency and to simplify the graphic presentation of the results.

Among the various possible underlying variograms, we have chosen to use the isotropic spherical variogram with a range of 15 pixels (much smaller than the dimension of the image to minimize the problem linked to statistical fluctuations) and with a sill of 1. The reason for this choice is that a specific simulation technique, based on the properties of the random tokens model, is known; this is simulated a follows:

– First we create a realization of a 3-D Poisson point process (I) with a constant density θ. Each point i of I is then considered as the centre of a sphere of constant radius R. The volume of each sphere is attributed a random value Z_i following a Gaussian distribution (0 mean and variance σ^2). The value $Z(x)$ finally simulated at each point of $\mathbb{R}^3$ is obtained by summing all the values attributed to the spheres intersected at x. The random function thus obtained has a zero mean and its covariance is isotropic and spherical, with a range which represents the diameter of the spheres and its sill calculated as follows:

$$C = \frac{\pi}{6}a^3\theta\sigma^2$$

Finally the Poisson intensity θ is directly linked to the statistical fluctuation. The larger the Poisson intensity, the smaller this fluctuation and, unfortunately, the longer the time needed for performing this simulation.

– A second particularity in this study is that we are looking for a 2-D simulation. It can obviously be obtained by looking at a section of a 3-D simulation. But a more realistic method consists in drawing the Poisson point process (I) as previously and in regarding each point as the centre of a disk. The difference is that the radius of the disk is no longer constant, as it corresponds to the intersection of a sphere located "at random" in $\mathbb{R}^3$ with a fixed plane.

The quality of the simulation can be appreciated by calculating the experimental variogram and by comparing it to the theoretical variogram. Figure 5 shows the reference simulation and the variograms calculated along the X and the Y directions (the angular tolerance is null) calculated on 50 steps of one pixel and the theoretical isotropic spherical variogram.

Once this is done, the next problem is to convolve the image by the appropriate convolution function p. Here this weighting function is derived from the sinc function as in references [4-6].

A naive solution is to discretize the function p (on a pixel basis) and to use these weights to perform a linear combination with the initial image. Unfortunately this assumes that the discretization of p is close enough to the theoretical convolution function. Moreover, the convoluted image is only available over the area of the initial image eroded by the diameter of the convolution function.

A second possibility is to recall that the covariance of a random tokens model is obtained as the convolution of the indicator function of the sphere (1 if the point belongs to the sphere S; 0 otherwise) denoted 1_S.

$$C(h) = \theta\sigma^2 1_S * 1_S$$

To obtain the convoluted covariance $Cp = C * P$, it is sufficient to implant "distorted" spheres $(1_S * p)$.

The usefulness of this construction comes from the fact that, for a given underlying spherical variogram, we can draw the point Poisson process once and for all. The initial spherical image is obtained by implanting spheres with a constant value (we will call it the "reference" image), the convolutions using two 1-D squared sinc weighting functions (diameters 3 and 10) are obtained by

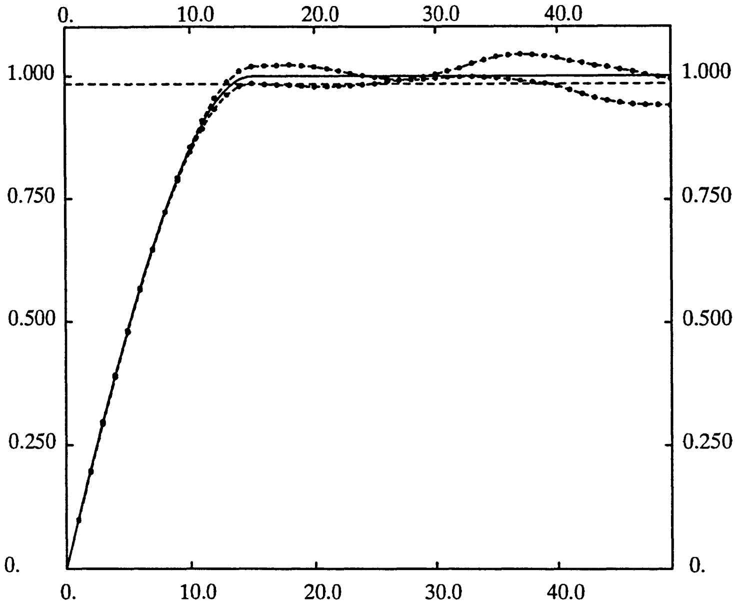

Fig. 5. — Theoretical and simulated variograms along X and Y.

distorting the spheres implanted at the same points. This will enable us to compare the image after deconvolution with the reference spherical image. Then several values of white noise ($C_0 = 0$, 0.05 and 0.2) are added to the convoluted images.

For each image, experimental variograms can be calculated and compared to the theoretical models.

Although the spherical variogram of the initial (non-convoluted) image was isotropic, the processed image is not isotropic, since the convolution function p only applies along the X direction. The larger the diameter of the convolution function, the stronger the geometric anisotropy. We can finally verify that the convolution changes the behaviour of the variogram at the origin from a linear shape to a smooth function.

4.2 DECONVOLUTION KRIGING OF THE SIMULATED IMAGES. — The next phase consists in performing the deconvolution and the noise filtering using the cokriging procedure. Again, we assume here that the deconvolution weighting function and the underlying structure are known. We must then determine the kriging neighbourhood, which will be the same for both diameters of the convolution weighting function and for the different values of the nugget effect. First an optimal 1-D neighbourhood radius of 10 pixels has been selected as a good compromise: it leads to a system with 21 kriging weights.

In the following figures (6 to 11), we first represent the reference image, followed by the image after the convolution and the addition of noise, and finally the image obtained by kriging. The dark edges of the last image correspond to the area where the deconvolution kriging and noise filtering cannot be performed as the neighbourhood would not be complete: their width is the neighbourhood radius R.

On the deconvoluted image, we can also calculate the variograms and compare them to the reference isotropic spherical variograms. In addition to the figures, we can check the efficiency of

the method by looking at the following resemblances:
- between the deconvoluted image and the reference image,
- between the deconvoluted variogram and the reference variogram illustrated by theoretical and experimental variograms calculated along X and Y,

As the process has been carried out on images, we can compare the theoretical SNR to the mean squared errors calculated between the reference image and the convoluted image (SNR0) and between the reference image and the deconvoluted image (SNR). These last two quantities will be called the experimental SNR. The experimental and theoretical SNR0 and SNR are summarized in the table III.

Table III.

	SNR0		SNR		I(R)	
	Theory	Experiment	Theory	Experiment	Theory	Experiment
Sinc(3)	19.642	16.445	44.577	31.490	2.270	1.915
Sinc(10)	5.213	4.990	10.012	9.344	1.921	1.873
Sinc(3) + 0.05	9.917	8.959	14.173	12.450	1.429	1.390
Sinc(10) + 0.05	4.136	3.964	7.074	6.589	1.710	1.662
Sinc(3) + 0.2	3.987	3.777	8.254	7.611	2.070	2.015
SInc(10) + 0.2	2.552	2.476	5.207	4.981	2.040	2.012

As we have already mentioned, the obvious conclusion is that the efficiency of the deconvolution decreases with the diameter of the convolution weighting function and the amount of nugget effect. The second remark is that there is good agreement between the experimental and the theoretical results.

If we look more carefully at the last deconvoluted image (diameter 10 and nugget effect 0.2) obtained with the 1-D neighbourhood (Fig. 11), we notice several artefacts, which appear as short horizontal stripes. Moreover, the same artefacts, which correspond to a residual 1-D convolution, appear on the experimental variogram, as a remaining smoothed behaviour along X, whereas its shape is linear along Y. The next attempt consists in performing the kriging procedure with a 2-D neighbourhood. The radius along X is the same as in the 1-D neighbourhood ($R_x = 10$) and the radius along Y is set to 1 pixel: the resulting kriging system consists of 63 kriging weights. The signal to noise ratio is improved and, this time, the deconvoluted image does not show the artefacts (Fig. 12 and Tab. IV).

Table IV.

	SNR0		SNR		I(R)	
	Theory	Experiment	Theory	Experiment	Theory	Experiment
1-D neighb.	2.552	2.476	5.207	4.981	2.040	2.012
2-D neighb.	2.552	2.476	6.253	6.008	2.442	2.427

To conclude this case study, we now assume that the convolution weighting function is known but we ignore the nature of the underlying variogram which is in practice unknown. The interactive procedure performed on the convoluted variograms shows a second possible fit (although less

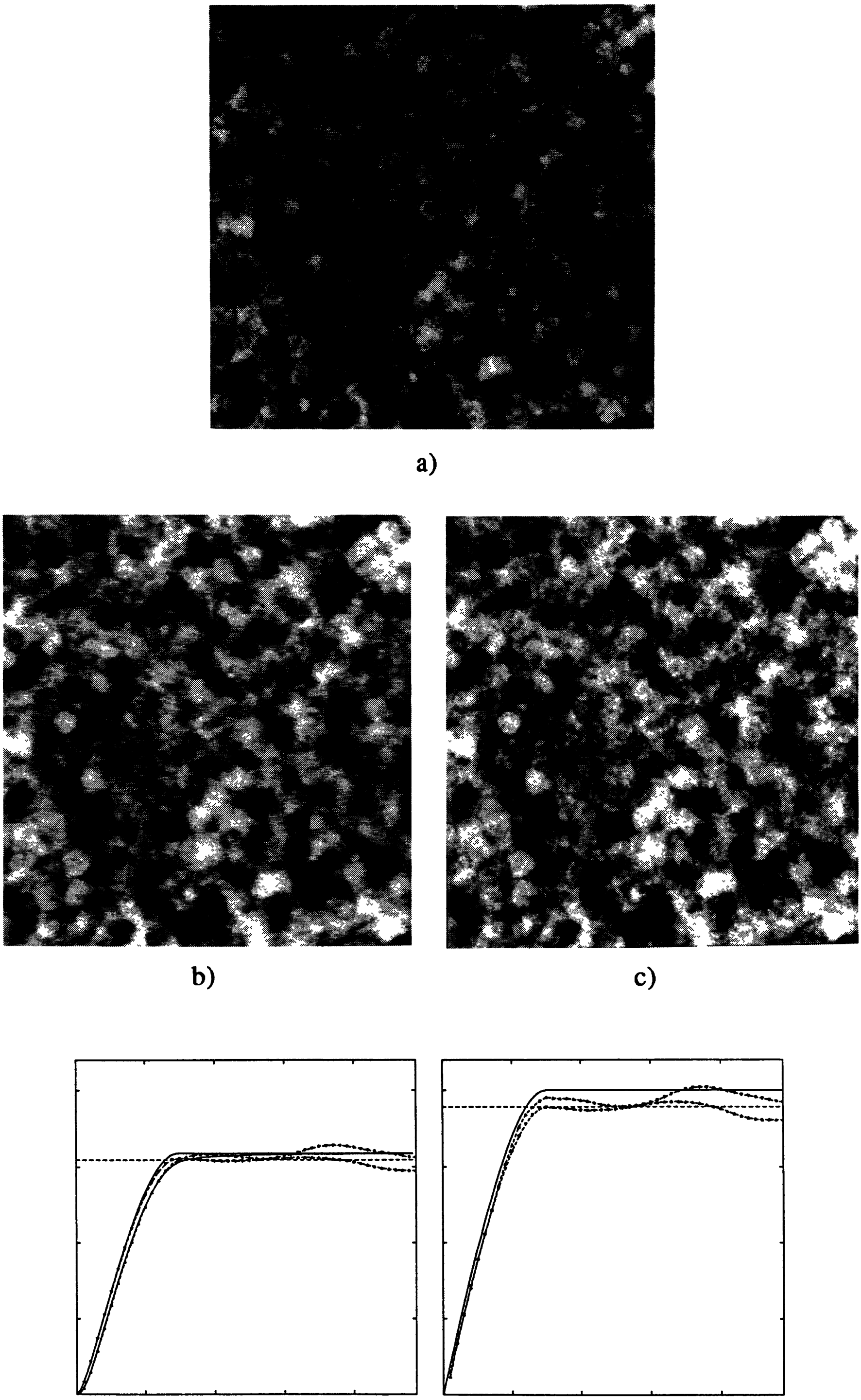

Fig. 6. — Convolution diameter $d = 3$. Nugget Effect $C_0 = 0$. Neighbourhood radius $R = 10$. SNR_0 : Theoretical 19.642, Experimental 16.445. SNR: Theoretical 44.577, Experimental 31.490. $I(R)$: Theoretical 2.270, Experimental 1.915.

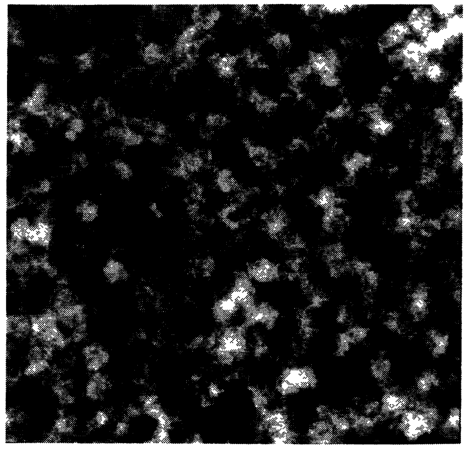

a)

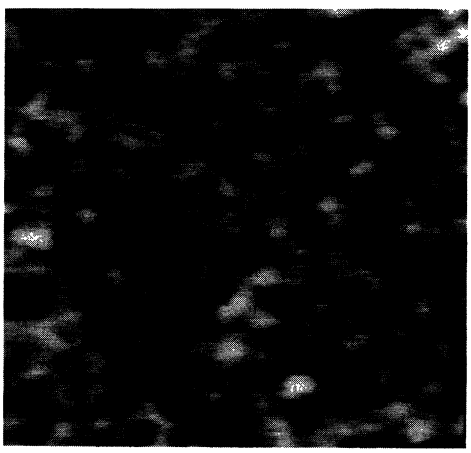

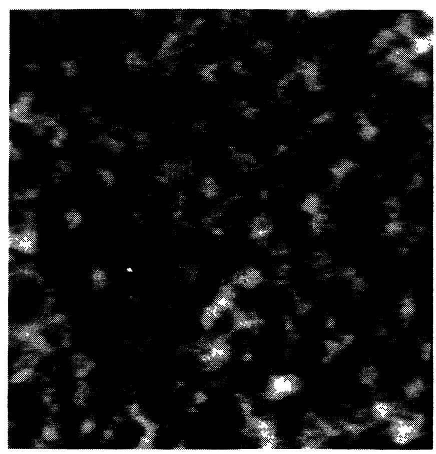

b) c)

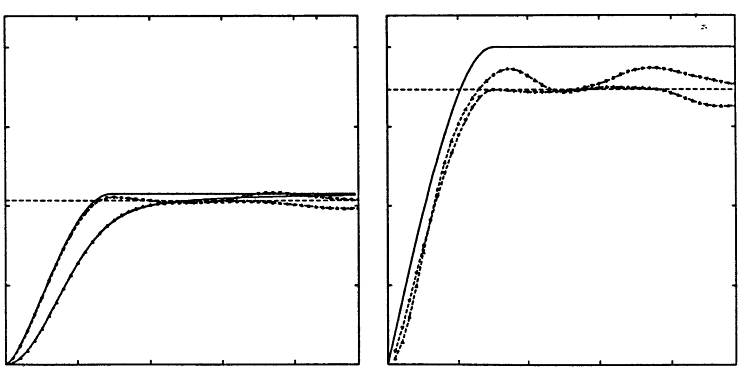

Fig. 7. — Convolution diameter $d = 10$. Nugget Effect $C_0 = 0$. Neighbourhood radius $R = 10$. SNR_0 : Theoretical 5.213, Experimental 4.990. SNR: Theoretical 10.012, Experimental 9.344. $I(R)$: Theoretical 1.921, Experimental 1.873.

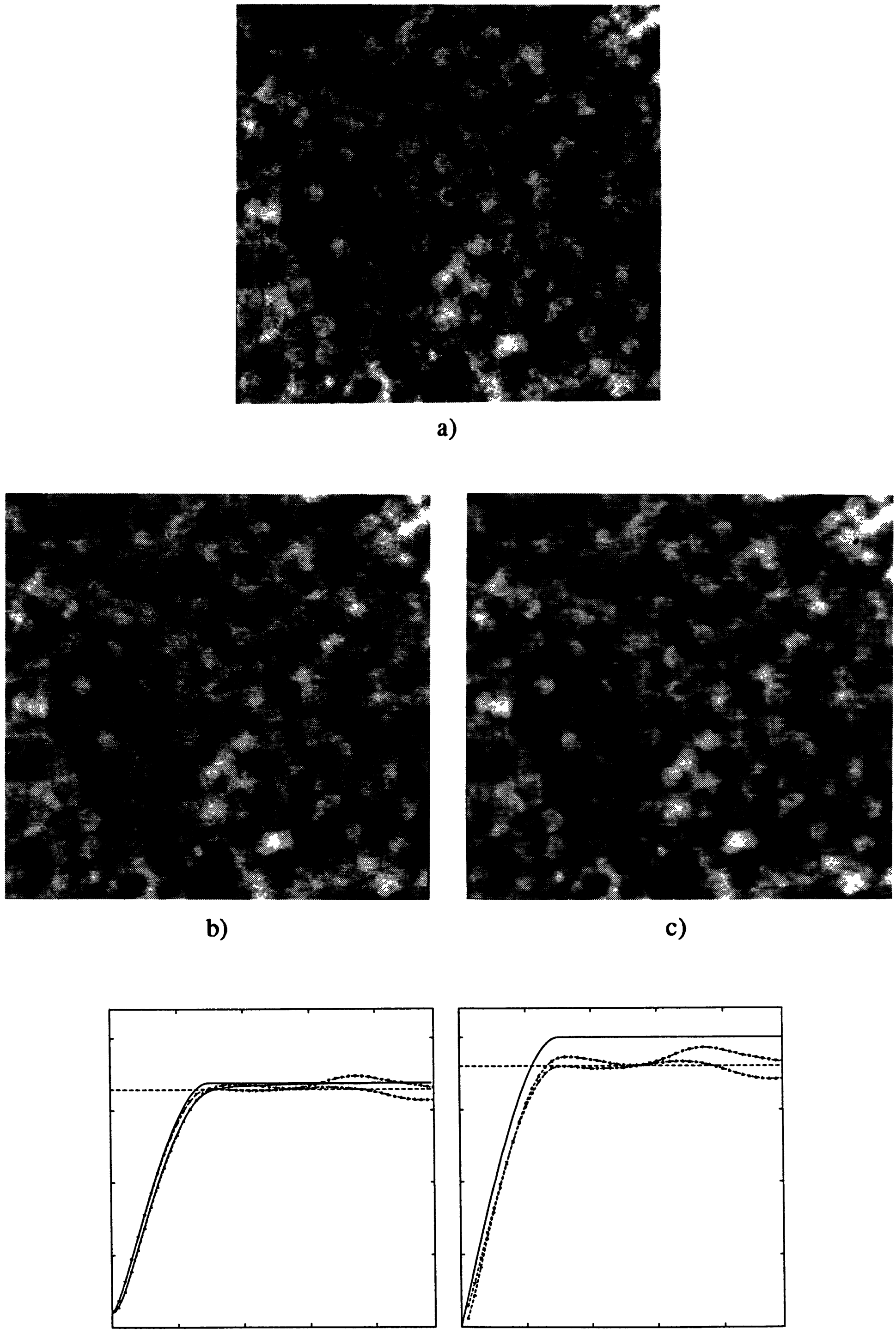

Fig. 8. — Convolution diameter $d = 3$. Nugget Effect $C_0 = 0.05$. Neighbourhood radius $R = 10$. SNR_0 : Theoretical 9.917, Experimental 8.959. SNR: Theoretical 14.173, Experimental 12.450. $I(R)$: Theoretical 1.429, Experimental 1.390.

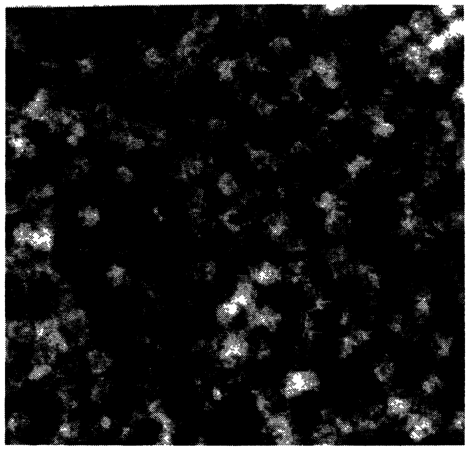

a)

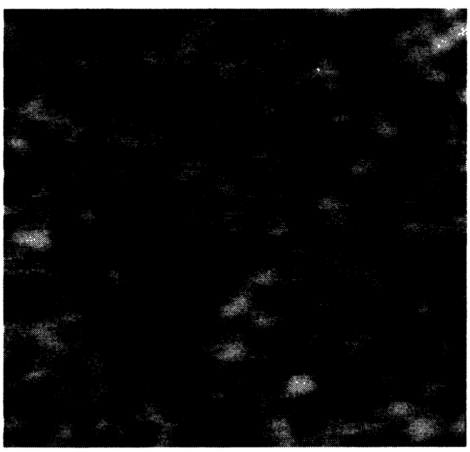

b)

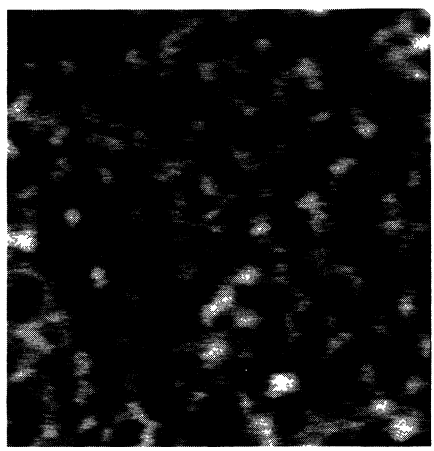

c)

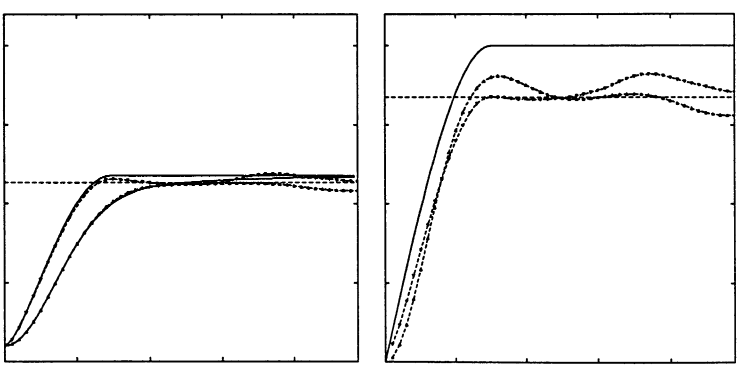

Fig. 9. — Convolution diameter $d = 10$. Nugget Effect $C_0 = 0.05$. Neighbourhood radius $R = 10$. SNR_0 : Theoretical 4.136, Experimental 3.964. SNR: Theoretical 7.074, Experimental 6.589. $I(R)$: Theoretical 1.710, Experimental 1.662.

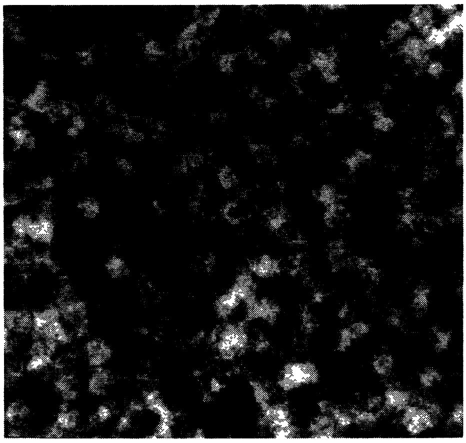

a)

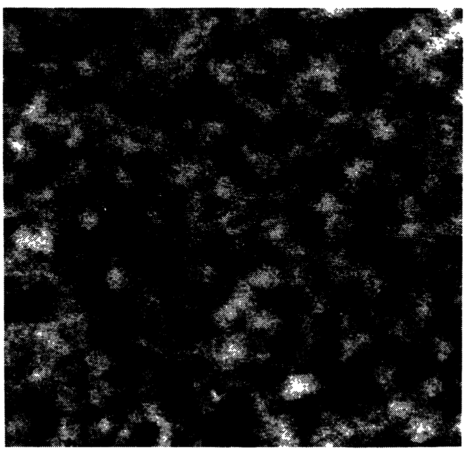

b)

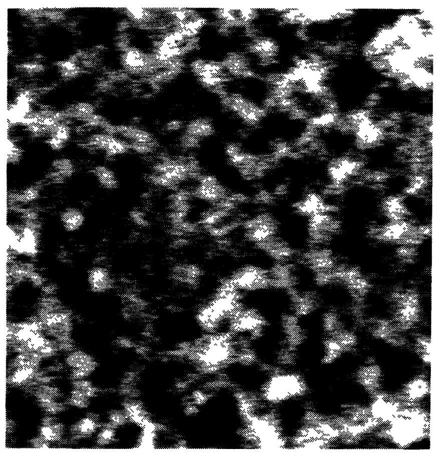

c)

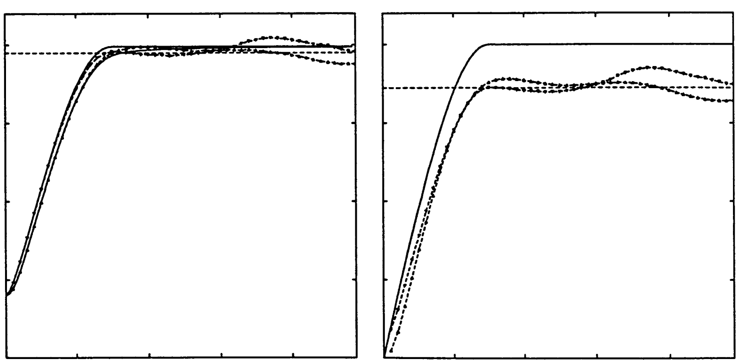

Fig. 10. — Convolution diameter $d = 3$. Nugget Effect $C_0 = 0.2$. Neighbourhood radius $R = 10$. SNR_0 : Theoretical 3.987, Experimental 3.777. SNR: Theoretical 8.254, Experimental 7.611. $I(R)$: Theoretical 2.070, Experimental 2.015.

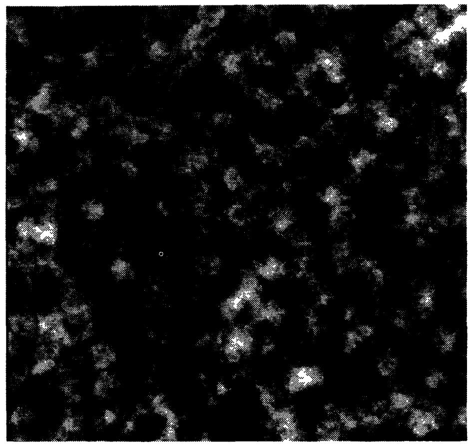

a)

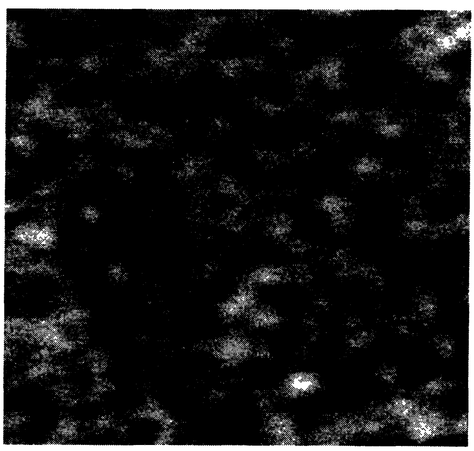

b)

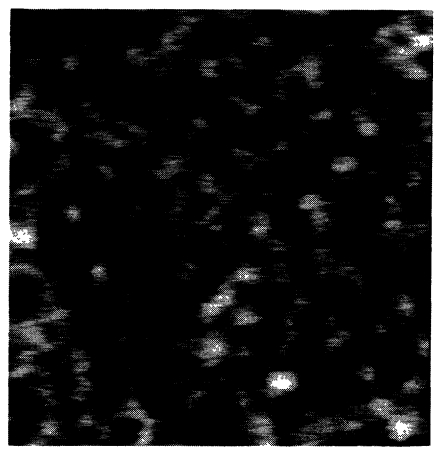

c)

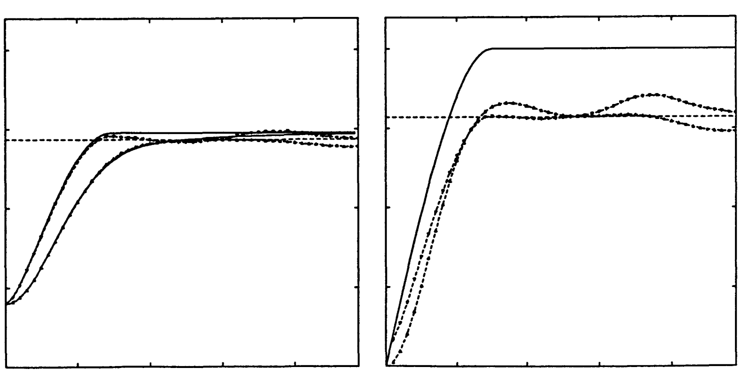

Fig. 11. — Convolution diameter $d = 10$. Nugget Effect $C_0 = 0.2$. Neighbourhood radius $R = 10$. SNR_0 : Theoretical 2.552, Experimental 2.476. SNR: Theoretical 5.207, Experimental 4.981. $I(R)$: Theoretical 2.040, Experimental 2.012.

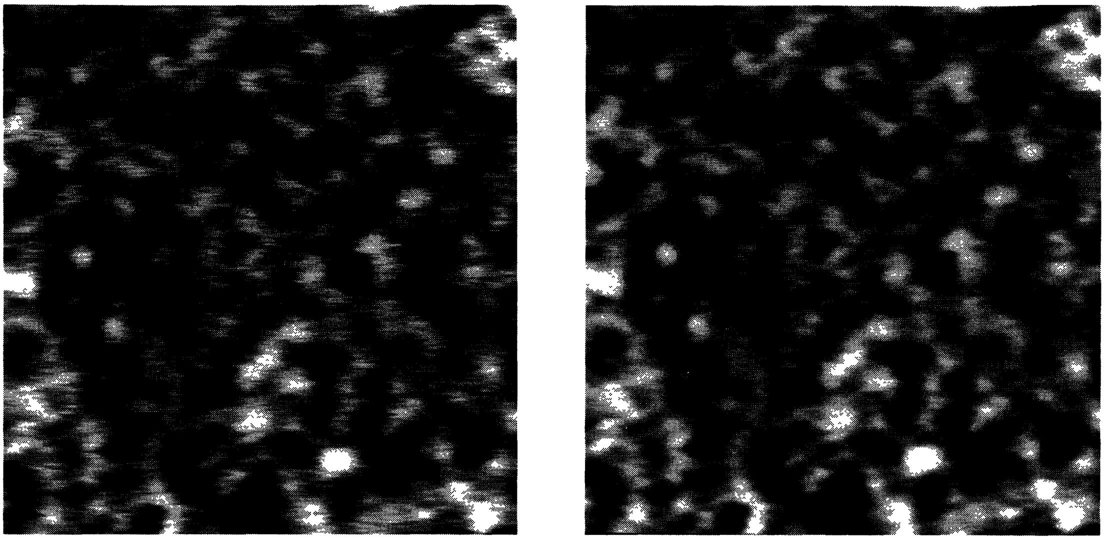

a) b)

Fig. 12. — Deconvolution kriging with 1-D (left) and 2-D (right) neighbourhoods.

accurate than the spherical variogram with a range of 15 and a sill of 1) with an underlying cubic variogram with a sill of 0.9 and a range of 17 (Fig. 13). The deconvolution kriging is performed with the 1-D neighbourhood and the following results are obtained (Tab. V).

Table V.

	SNR0		SNR		I(R)	
	Theory	Experiment	Theory	Experiment	Theory	Experiment
Spherical	2.552	2.476	5.207	4.981	2.040	2.012
Cubic	3.109	2.476	9.473	4.981	3.047	2.012

Despite a wrong choice of the underlying variogram model, the deconvolution procedure led to results (SNR and $I(R)$) very close to those corresponding to the "true" model. We must however point out that the theoretical results are quite different, as they strongly depend on the model.

The images are strictly similar and therefore have not been presented here. And this is precisely what the user expects from a robust deconvolution procedure !

4.3 APPLICATION TO A REAL CASE. — This approach was used with real data obtained on a biological specimen with a confocal optical microscope giving three-dimensional images. In this case there is a strong convolution in the Z direction (depth of the specimen) and the weighting function is derived from the sinc function as used in the previous simulated data set. The results of the deconvolution are satisfactory, and are reported in [4-6].

In our presentation and in the application mentioned, we used one-dimensional convolutions. The same approach can be followed for three-dimensional convolutions, involving longer calculations for the convoluted variogram. However, in many practical cases, these are just an iteration

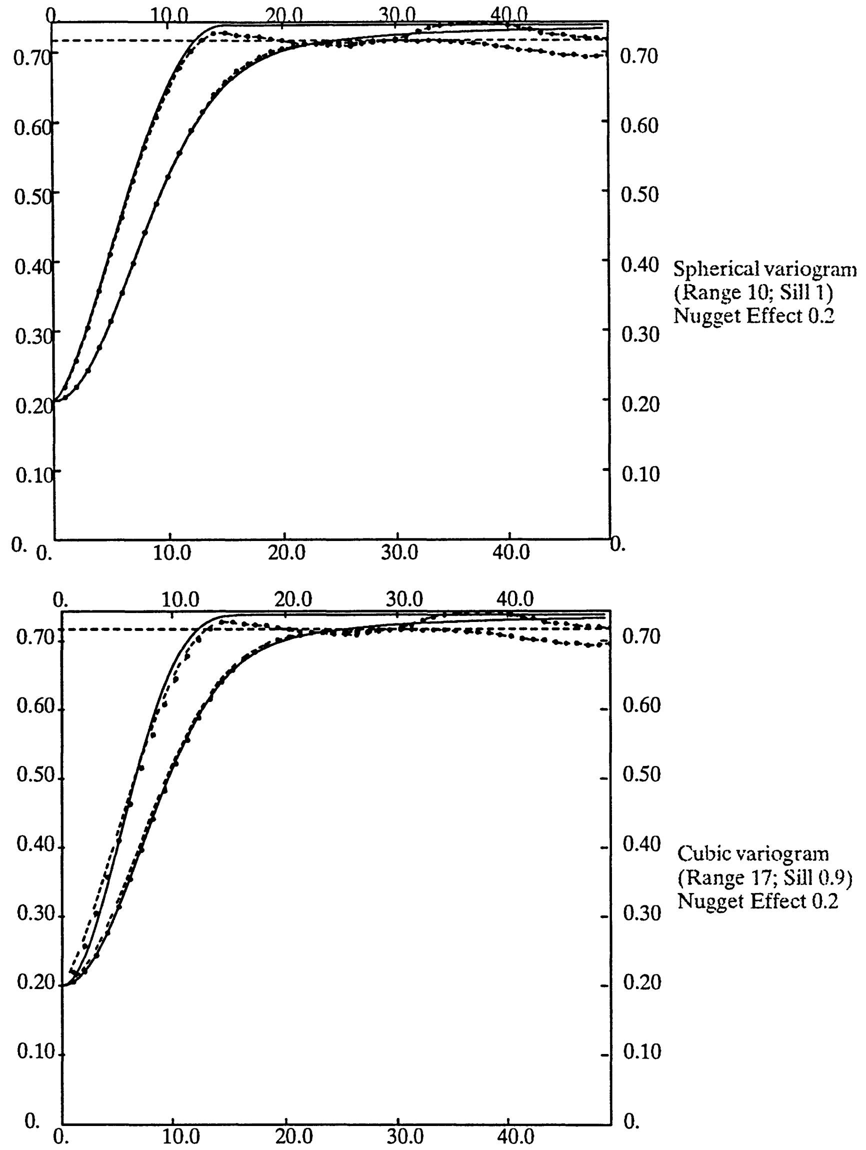

Fig. 13. — Spherical and cubic variogram fits.

of three one-dimensional convolutions on three orthogonal directions. Lower initial SNR are expected, since there is a higher degradation of the data. The expected improvement of the SNR can be calculated as before.

5. Conclusion.

This study of the deconvolution of data by kriging enables us to draw the following conclusions:

- efficient and easy deconvolutions can be obtained, even in the presence of noise. As a result of the minimization of the variance of estimation, the choice of weights from the kriging system gives a good compromise between the operation close to a differentiation required for the deconvolution, and the smoothing required for noise filtering. This is an effect of the adaptive properties of kriging filters.

- from some simulations, the deconvolution seems to be robust with respect to the choice of the model of the underlying variogram (provided that the variogram of the data is not too different from the calculated convoluted variogram). On the other hand, the calculated SNR (and its expected improvement) strongly depends on the model, and so must be used with some care in the applications.

This procedure could contribute to increase the quality of various images obtained in electron microscopy and microprobe at a high magnification.

References

[1] PRATT W.K., Digital Image Processing, (J. Wiley, New-York, 1978).

[2] PINNAMANENI B.P., JEULIN D., DALY C., MORY C., TENCÉ M., COLLIEX C., Multispectral linear filtering of high resolution EELS images by Geostatistics, *Microsc. Microanal. Microstruct.* **2** (1991) 107-127.

[3] DALY C., JEULIN D. and LAJAUNIE C., Application of multivariate kriging to the processing of noisy images, in: Geostatistics, M. Armstrong Ed., Vol 2, Kluwer Academic Publishers, Dordrecht, 1989, pp. 749-760.

[4] CONAN V., HOWARD C.V., JEULIN D., RENARD D. and CUMMINS P., Improvements of 3D confocal microscope images by geostatistical filters, *Trans. Roy. Mic. Soc.* 1 (1990) 281-284.

[5] CONAN V., Improvements of 3D confocal images by geostatistical filters (Paris School of Mines Publication, 1990).

[6] CONAN V., GESBERT S., HOWARD C.V., JEULIN D., MEYER F. and RENARD D., Geostatistical and morphological methods applied to 3D microscopy, *J. Microsc.* **166** (1992) 169-184.

[7] SHAW P.J., Three-dimensional optical microscopy using tilted views, *J. Microsc.* **158** (1990) 165-172.

[8] TIKHONOV A., ARSÉNINE V., Méthodes de résolution de problèmes mal posés (MIR, Moscou, 1974).

[9] MATHERON G., Les variables régionalisées et leur estimation (Masson, Paris, 1965).

[10] MATHERON G., The theory of regionalised variables and its applications, Cahiers du Centre de Morphologie Mathématique, Fasc. 5, ENSMP, Paris (1970).

[11] SÉGURET S., Pour une méthodologie de déconvolution de variogrammes (Paris School of Mines Publication, 1988).

[12] LE LOCH G., Deconvolution d'images scanner. Partie II: Krigeage déconvoluant (Paris School of Mines Publication, 1990).

[13] DALY C., Applications de la géostatistique à quelques problèmes de filtrage, Thèse de Docteur en Géostatistique, ENSMP (Juin 1991) 235 p.

[14] DALY C., JEULIN D., BENOIT D., Nonlinear statistical filtering and applications to segregation in steels from microprobe images. Communication présentée à Tenth Pfefferkorn Conference on Signal and Image Processing in Microscopy and Microanalysis, 16-19 Sept. (Cambridge, U.K.) To be published in *Scanning Microscopy Supplement* **6** (1992).

[15] MATHERON G., A simple substitute for conditional expectation: the disjunctive kriging. In: Advanced Geostatistics in the Mining Industry, M. Guarascio Ed. (Dordrecht, Holland: D. Reidel Publ. Co.) *NATO ASI Series C* **24** (1976) 221-236.

[16] MATHERON G., The intrinsic random functions, and their applications, *Adv. Appl. Prob.* **5** (1973) 439-468.

[17] JANSSON P.A., Deconvolution with applications on spectroscopy (Academic Press, London, 1984) pp. 69-135.

[18] AGARD D.A., HIRAOKA Y., SHAW P., SEDAT J.W., Fluorescence microscopy in 3 dimensions, *Methods Cell. Biol.* **30** (1989) 353-377.

[19] SHAW P., HIGHETT M., RAWLINS D., Confocal microscopy and image processing in the study of plant nuclear structure, **166** (1992) 87-97.

[20] BLUEPACK 3-D - MAGMA Software Package, Centre de Géostatistique, Ecole de Mines de Paris.

6. APPENDIX

Spherical variogram (Range 15; Sill 1)
Exponential convolution function
Nugget Effect = 0.01

Diameter	SNR0	SNR	I(R)
1.	16.599	20.190	1.216
2.	8.841	13.678	1.547
3.	5.915	10.797	1.825
5.	3.585	7.927	2.211
10.	2.073	5.096	2.458

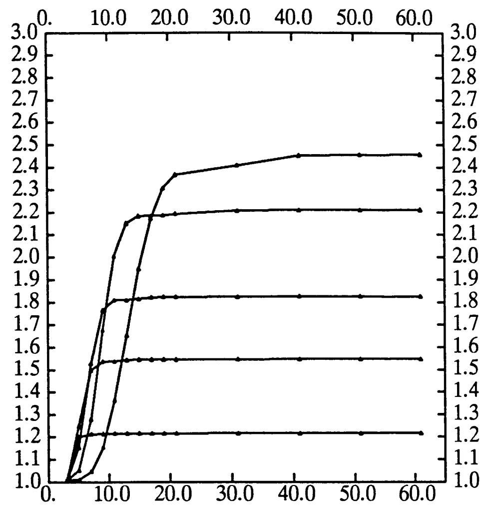

Spherical variogram (Range 15; Sill 1)
Exponential convolution function
Nugget Effect = 0.05

Diameter	SNR0	SNR	I(R)
1.	9.976	12.721	1.275
2.	6.532	9.329	1.428
3.	4.783	7.585	1.586
5.	3.135	5.731	1.828
10.	1.914	3.561	1.861

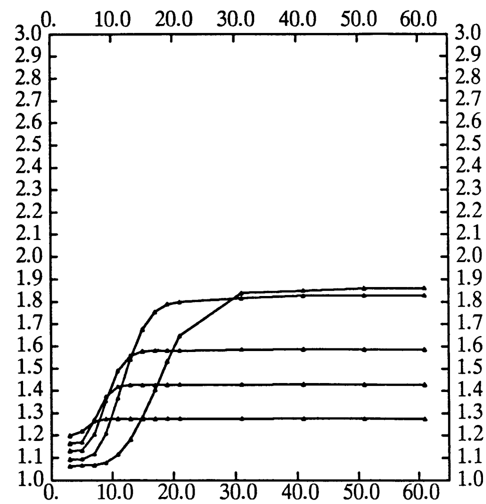

Spherical variogram (Range 15; Sill 1)
Exponential convolution function
Nugget Effect = 0.10

Diameter	SNR0	SNR	I(R)
1.	6.656	10.127	1.521
2.	4.934	7.738	1.568
3.	3.860	6.415	1.662
5.	2.710	4.872	1.798
10.	1.747	3.021	1.729

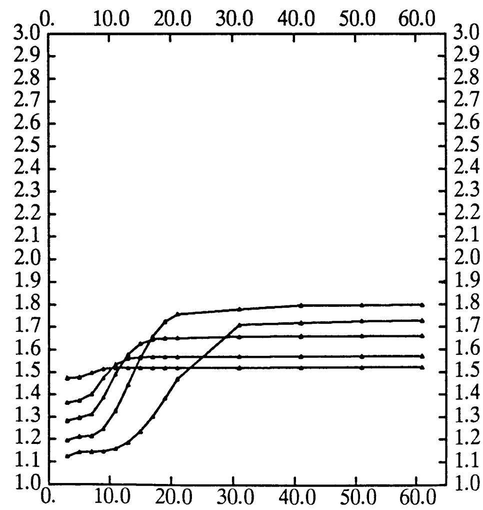

Spherical variogram (Range 15; Sill 1)

Uniform convolution function

Nugget Effect = 0.01

Diameter	SNR0	SNR	I(R)
1.	22.878	24.198	1.058
2.	12.873	16.942	1.316
3.	8.914	13.169	1.478
5.	5.441	9.599	1.764
10.	2.574	4.827	1.875

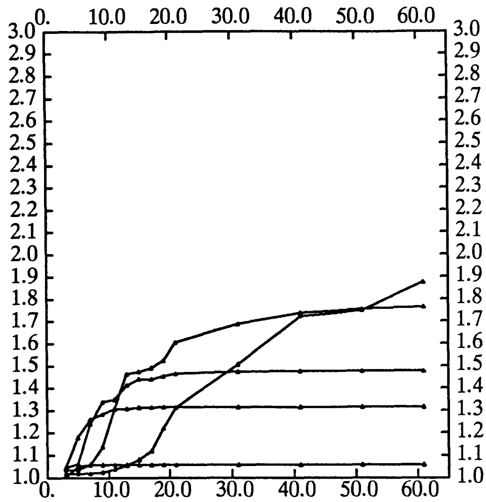

Spherical variogram (Range 15; Sill 1)

Uniform convolution function

Nugget Effect = 0.05

Diameter	SNR0	SNR	I(R)
1.	11.946	15.594	1.305
2.	8.497	12.101	1.424
3.	6.571	9.792	1.490
5.	4.468	7.256	1.624
10.	2.334	3.930	1.684

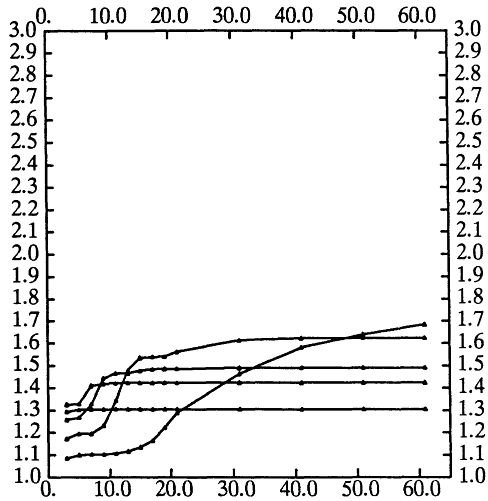

Spherical variogram (Range 15; Sill 1)

Uniform convolution function

Nugget Effect = 0.10

Diameter	SNR0	SNR	I(R)
1.	7.479	12.091	1.617
2.	5.964	9.947	1.668
3.	4.946	8.322	1.683
5.	3.652	6.401	1.753
10.	2.089	3.549	1.699

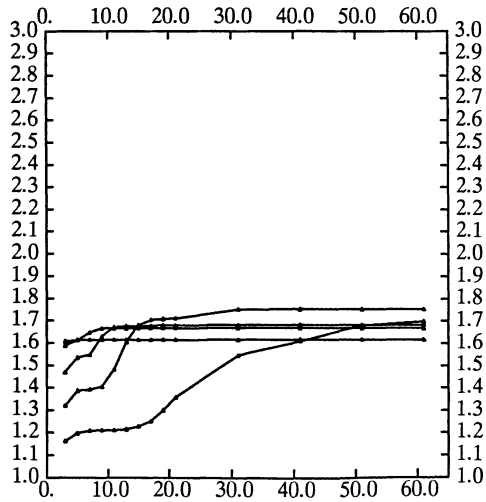

Spherical variogram (Range 15; Sill 1)
Gaussian convolution function
Nugget Effect = 0.01

Diameter	SNR0	SNR	I(R)
1.	17.966	20.870	1.162
2.	9.741	13.422	1.378
3.	6.565	9.931	1.513
5.	3.817	6.765	1.772
10.	1.979	3.209	1.786

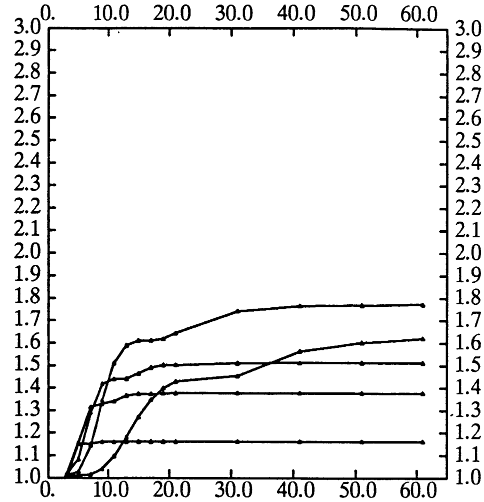

Spherical variogram (Range 15; Sill 1)
Gaussian convolution function
Nugget Effect = 0.05

Diameter	SNR0	SNR	I(R)
1.	10.453	13.699	1.311
2.	7.010	9.893	1.411
3.	5.200	7.744	1.489
5.	3.312	5.509	1.663
10.	1.834	2.719	1.483

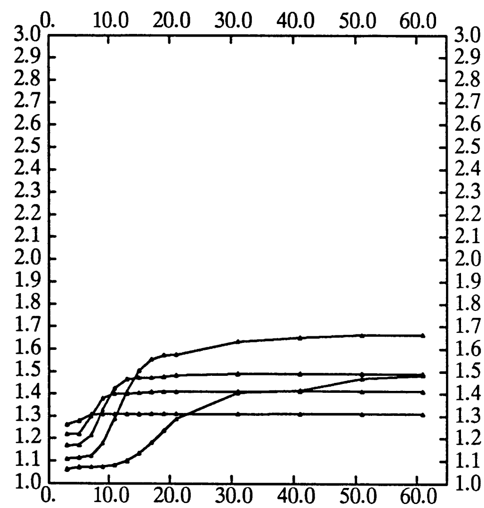

Spherical variogram (Range 15; Sill 1)
Gaussian convolution function
Nugget Effect = 0.10

Diameter	SNR0	SNR	I(R)
1.	6.865	10.886	1.586
2.	5.191	8.325	1.604
3.	4.127	6.759	1.638
5.	2.841	4.875	1.716
10.	1.680	2.504	1.490

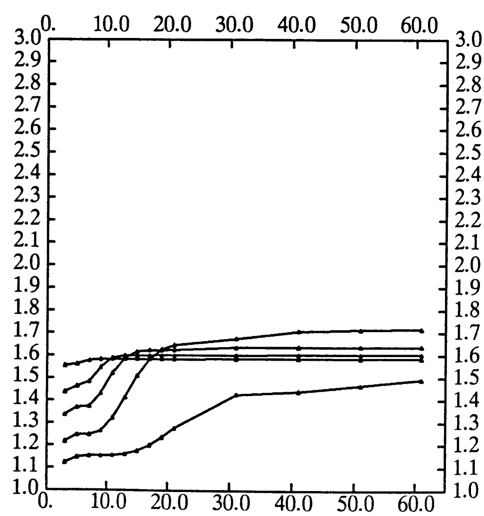

Cubic variogram (Range 15; Sill 1)
Exponential convolution function
Nugget Effect = 0.01

Diameter	SNR0	SNR	I(R)
1.	59.214	134.412	2.270
2.	19.178	76.407	3.984
3.	9.128	50.517	5.534
5.	4.232	25.832	6.104
10.	2.140	8.530	3.986

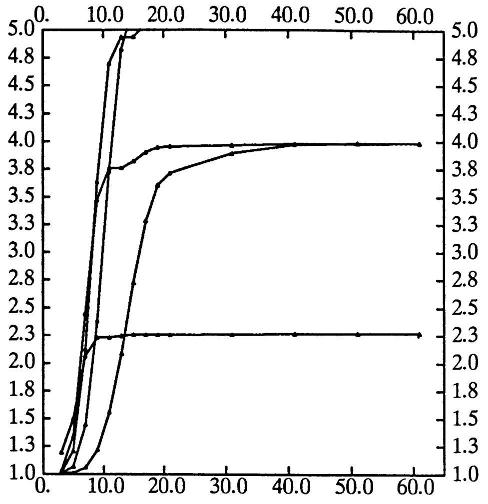

Cubic variogram (Range 15; Sill 1)
Exponential convolution function
Nugget Effect = 0.05

Diameter	SNR0	SNR	I(R)
1.	17.578	48.654	2.768
2.	10.853	32.256	2.972
3.	6.687	21.894	3.274
5.	3.619	11.388	3.147
10.	1.971	4.449	2.257

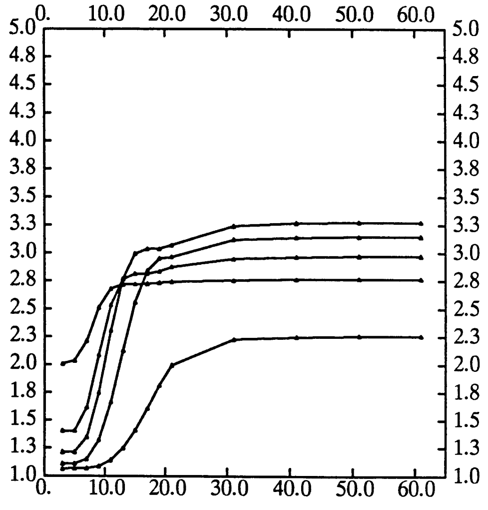

Cubic variogram (Range 15; Sill 1)
Exponential convolution function
Nugget Effect = 0.10

Diameter	SNR0	SNR	I(R)
1.	9.356	22.147	2.367
2.	7.035	21.272	3.024
3.	5.011	14.737	2.941
5.	3.065	8.030	2.620
10.	1.794	3.486	1.943

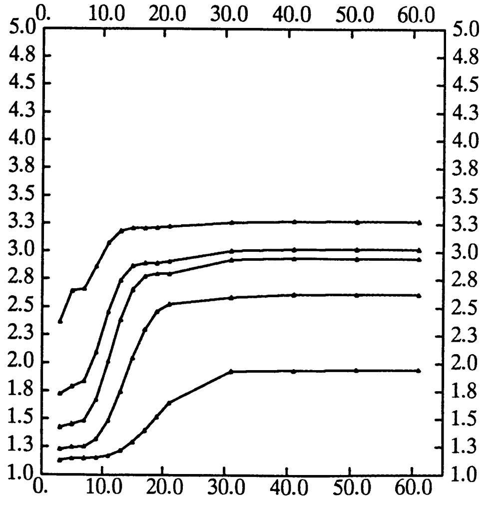

Cubic variogram (Range 15; Sill 1)

Uniform convolution function

Nugget Effect = 0.01

Diameter	SNR0	SNR	I(R)
1.	91.761	180.984	1.972
2.	60.609	124.177	2.049
3.	32.680	78.422	2.400
5.	10.738	37.472	3.490
10.	2.586	6.844	2.647

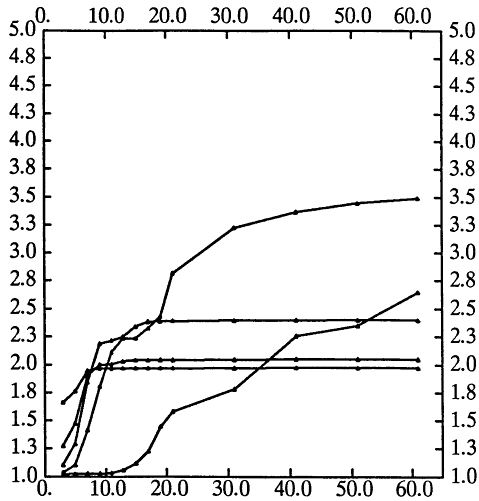

Cubic variogram (Range 15; Sill 1)

Uniform convolution function

Nugget Effect = 0.05

Diameter	SNR0	SNR	I(R)
1.	19.647	59.058	3.006
2.	17.699	48.917	2.764
3.	14.164	37.969	2.681
5.	7.512	20.677	2.753
10.	2.343	5.099	2.176

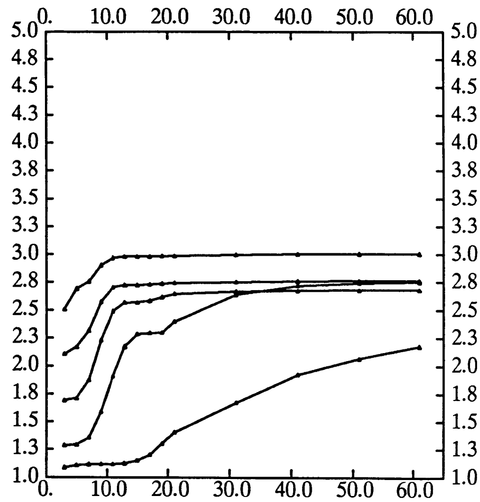

Cubic variogram (Range 15; Sill 1)

Uniform convolution function

Nugget Effect = 0.10

Diameter	SNR0	SNR	I(R)
1.	9.911	35.773	3.609
2.	9.390	31.202	3.323
3.	8.292	25.619	3.090
5.	5.461	15.167	2.777
10.	2.098	4.345	2.071

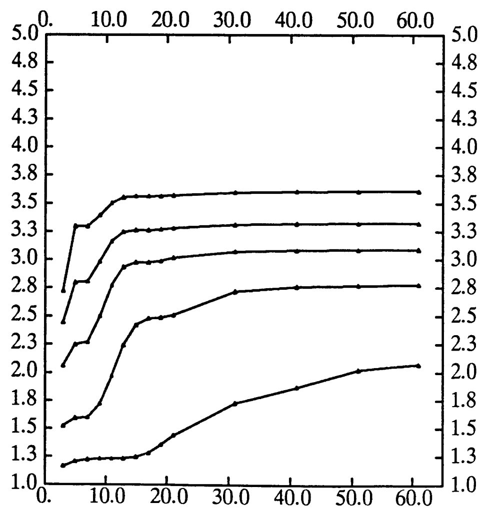

Cubic variogram (Range 15; Sill 1)

Gaussian convolution function

Nugget Effect = 0.01

Diameter	SNR0	SNR	I(R)
1.	82.089	184.181	2.244
2.	32.036	117.434	3.666
3.	13.174	66.019	5.011
5.	4.692	17.717	3.776
10.	1.997	3.562	1.784

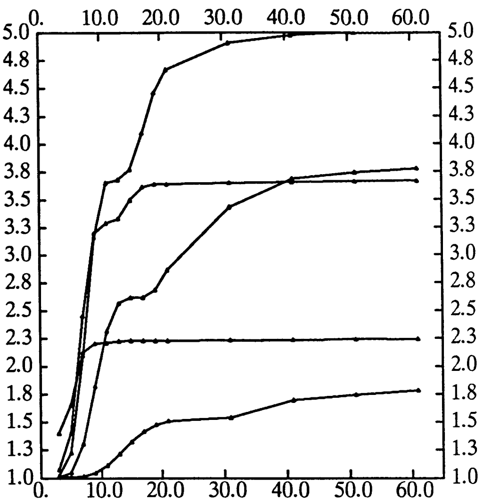

Cubic variogram (Range 15; Sill 1)

Gaussian convolution function

Nugget Effect = 0.05

Diameter	SNR0	SNR	I(R)
1.	19.164	56.713	2.959
2.	14.042	42.644	3.037
3.	8.627	27.637	3.204
5.	3.951	9.994	2.529
10.	1.849	2.879	1.557

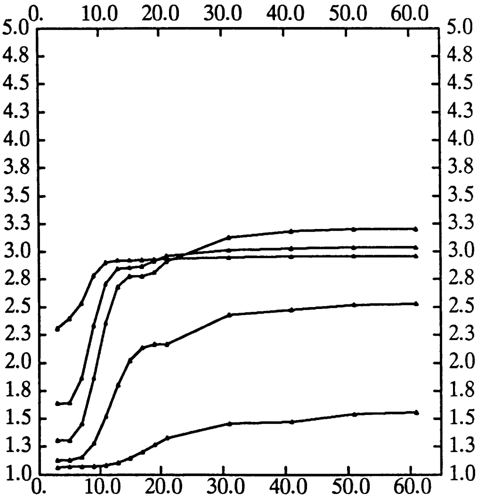

Cubic variogram (Range 15; Sill 1)

Gaussian convolution function

Nugget Effect = 0.10

Diameter	SNR0	SNR	I(R)
1.	9.786	34.338	3.509
2.	8.250	26.932	3.264
3.	6.027	18.331	3.041
5.	3.299	7.679	2.328
10.	1.693	2.612	1.543